Phys. Status Solidi A **213,** No. 12, 3238–3244 (2016) / **DOI** 10.1002/pssa.201600511

physica status solidi a
www.pss-a.com
applications and materials science

Self-assembled peptide nanofiber templated ALD growth of TiO_2 and ZnO semiconductor nanonetworks

Ruslan Garifullin[1,2], Hamit Eren[1], Turkan G. Ulusoy[1], Ali K. Okyay[,1,3], Necmi Biyikli[***,1], and Mustafa O. Guler[*,1]**

[1] Institute of Materials Science and Nanotechnology, National Nanotechnology Research Center (UNAM), Bilkent University, 06800 Ankara, Turkey
[2] Institute of Fundamental Medicine and Biology, Kazan Federal University, 18 Kremlyovskaya St., 420008 Kazan, Russia
[3] Department of Electrical and Electronics Engineering, Bilkent University, 06800 Ankara, Turkey

Received 2 June 2016, accepted 17 August 2016
Published online 7 September 2016

Keywords atomic layer deposition, metal oxide semiconductors, nanofibers, nanomaterials, peptides, self-assembly

* Corresponding author: e-mail moguler@unam.bilkent.edu.tr, Phone: +90 (312) 290 8986, Fax: +90 (312) 266 4365
** e-mail aokyay@ee.bilkent.edu.tr
*** e-mail biyikli@unam.bilkent.edu.tr

Here peptide amphiphile (PA) nanofiber network is exploited as a three-dimensional soft template to construct anatase TiO_2 and wurtzite ZnO nanonetworks. Atomic layer deposition (ALD) technique is used to coat the organic nanonetwork template with TiO_2 and ZnO. ALD method enables uniform and conformal coatings with precisely controlled TiO_2 and ZnO thickness. The resulting semiconducting metal oxide nanonetworks are utilized as anodic materials in dye-sensitized solar cells. Effect of metal oxide layer thickness on device performance is studied. The devices based on thin TiO_2 coatings (<10 nm) demonstrate considerable dependence on material thickness, whereas thicker (>17 nm) ZnO-based devices do not show an explicit correlation.

1 Introduction There are mainly two basic approaches in nanostructured materials synthesis [1]. The first one is a top-down approach and requires material removal from the bulk precursor material by chemical, mechanical, or thermal means; acid etching, focused ion milling, and laser ablation are among these top-down synthesis techniques [2]. It is a straightforward, albeit poor in material architecture control, method that has established its niche in nanostructured materials synthesis. On the other hand, bottom-up approach exploits fine-tuned materials assembly. Bottom-up approach is realized via direct self-assembly of target nanostructures or material growth on synthetic or natural nanotemplates. Bottom-up nanostructured materials synthesis offers considerably wider spectrum of achievable material architectures and structural hierarchies. Synthesis of nanostructured materials on self-assembled soft nanotemplates is of significant importance because many biological systems utilize a similar approach to construct complex biomolecule-templated materials [3].

Peptide amphiphile (PA) molecules with their intrinsic property to self-assemble into nanostructures such as fibers, present a versatile tool in inorganic material templating [4]. The PAs were used as soft nanoscale templates in several studies for fabrication of inorganic nanomaterials [5]. Most of these studies are focused on in-solution material deposition on the surface of a template. Even though this approach allows successful material deposition [6], precise control over material thickness, uniformity, and high conformality is difficult to achieve in a repeatable manner. In this work, in order to circumvent this challenge, atomic layer deposition (ALD) technique was deployed in material growth over PA nanonetwork template [7]. ALD involves low-temperature iterative material deposition from vapor phase in a self-limiting fashion. In each deposition cycle, Ti- or Zn- containing volatile metalorganic complexes form a self-limiting uniform monolayer that consequently reacts with water vapor (H_2O) as an oxygen precursor. ALD approach allowed formation of TiO_2 or ZnO nanonetworks

with tunable wall thickness and high template conformality. Template conformality and coating uniformity were achieved through operating ALD reactor in exposure mode. This mode ensured sufficient diffusion of the precursors into highly porous three-dimensional template. The metal oxide and peptide hybrid nanomaterials were used for TiO_2 nanotube formation. The organic template was removed by calcination at 450 °C where amorphous titania transforms to anatase form. ZnO-peptide hybrid nanomaterials were not thermally processed, as ZnO readily grows in crystalline wurtzite form during the ALD process. In principle, nanostructured anatase TiO_2 and wurtzite ZnO are wide bandgap semiconductors and can be used as photoanode materials. Nanostructured anodic materials [8] attract great interest as the matter at nanoscale regime can provide considerable enhancement in charge carrier separation, charge carrier transport and active surface area. Nanostructured metal oxides such as TiO_2 [9], ZnO [10], SnO_2 [11], Nb_2O_5 [12], and Ta_2O_5 [13] have found wide applications in solar energy utilization.

Here we show fabrication of nanostructured TiO_2 and ZnO on self-assembled peptide nanofiber soft template. As a proof of principle, we utilized semiconducting TiO_2 and ZnO in assembly of dye sensitized solar cells and studied material thickness effect on device performance in terms of open-circuit voltage (V_{oc}), short circuit-current (J_{sc}), and fill factor. Three sets of nanostructured photoanodes with different TiO_2 deposition cycles (100, 150, and 200) and different ZnO deposition cycles (100, 125, and 150) were fabricated. TiO_2 and ZnO nanonetworks in photoanodes form a system of interconnected nanotubes, which can facilitate electron transfer. Moreover, these networks are porous high-surface-area materials and they can drastically increase number of sensitizer molecules attached to the semiconductor material surface.

2 Experimental

2.1 Materials Fmoc- and Boc- protected amino acids, Rink Amide MBHA resin, and HBTU were purchased from NovaBiochem and ABCR. Other chemicals were purchased from Fisher, Merck, Alfa Aesar, or Aldrich and used as received. The 2.2 mm thick fluorine doped tin oxide (FTO) coated glass (sheet resistivity of $7\,\Omega\,sq^{-1}$), Ruthenizer 535-bis TBA (N719) photosensitizer dye, Iodolyte AN 50 electrolyte, and Meltonix 1170-60 thermoplastic were purchased from Solaronix.

2.2 Peptide synthesis and characterization Peptide molecules (Fig. S1) were synthesized by solid phase peptide synthesis method. Peptide sequence was constructed on Rink Amide MBHA resin ($0.59\,mmol\,g^{-1}$). 0.5 mmol peptide synthesis was carried out; two equivalents (with respect to resin) of amino acids and lauric acid were used in each coupling. Amino acids or lauric acid (2 eq.) were activated with DIPEA (3 eq.) and HBTU (1.98 eq) prior to coupling. All couplings were carried out in dimethylformamide (DMF). At the end of the coupling cycles, resin was cleaved from the resin by concentrated trifluoroacetic acid (TFA). For this purpose, a 10 mL cleavage cocktail (TFA:TIS:H_2O = 9.5:0.25:0.25) was prepared; Milli-Q water (H_2O) and triisopropylsilane (TIS) were used as scavengers. Cleaved peptide was collected by dichloromethane (DCM), which was later removed alongside with TFA by rotary evaporation. Residual material was triturated by cold diethyl ether. White peptide precipitate was completely separated from ether by centrifugation; the centrifugate was dissolved in water, deep freezed at −80 °C and finally lyophilized. Lyophilized peptide was characterized by high resolution time-of-flight mass spectrometer coupled to liquid chromatography system (Agilent 1200/6210) (Figs. S2, S3, SI).

2.3 Photoanode fabrication and characterization First, fluorine doped tin oxide (FTO) glass (1.67 cm × 1.67 cm) was treated with 100 mL of H_2O:NH_4OH:H_2O_2 (5:1:1) solution at 75 °C for 30 min. Then, 4 μL of 2% (wt v^{-1}) peptide amphiphile solution was spread directly on FTO with restricted area of 0.09π cm^2 (~0.28 cm^2), afterwards peptide solution was gelled by NH_3 vapor in closed container. Obtained hydrogel was converted to alcogel by series of gradual alcohol in water mixtures (15, 30, 45, 60, 75, 90, and 100%); finally, alcogel was converted to aerogel by critical point drying. Next, ALD was employed to deposit TiO_2 or ZnO in a commercial thermal ALD reactor (Ultratech Inc. Savannah S100). The substrate temperature was kept at 150 °C during the ALD process using $Ti(NMe_2)_4$, $Zn(Et)_2$, and H_2O as titanium, zinc, and oxygen precursors, respectively. Prior to deposition, $Ti(NMe_2)_4$ precursor was preheated to 75 °C. As a carrier gas, N_2 was employed with a flow rate of 20 sccm. The reactor was operated in exposure mode: dynamic vacuum was switched to static vacuum just before precursor introduction, and after certain exposure time (60 s) again back to dynamic vacuum just before N_2 purge. The deposition was carried out using successive three different numbers of deposition cycles including 100, 150, and 200 cycles of TiO_2, and 100, 125, and 150 cycles of ZnO. As-synthesized TiO_2 samples were calcined in accordance with the following procedure: ramp from 25 to 150 °C with 5 °C min^{-1}, from 150 to 350 °C with 1 °C min^{-1}, from 350 to 450 °C with 5°C min^{-1} and wait for 30 min. FEI Quanta 200 FEG scanning electron microscope with EDX attachment was used to study morphology and chemical composition of TiO_2 and ZnO nanonetworks. Peptide aerogel was sputter coated with 6 nm of Pt prior to SEM imaging. FEI Tecnai G2 F30 transmission electron microscope was used to obtain TEM micrographs. PANalytical X'Pert powder X-ray diffractometer was used to analyze crystal structures of TiO_2 and ZnO nanonetworks. Cary 5000 UV-Vis-NIR spectrophotometer with an internal diffuse reflectance attachment was used to record diffuse reflectance spectra of TiO_2 and ZnO. WITec Alpha 300S scanning near-field optical microscope with Raman module was used to characterize the samples. Calcined TiO_2 and

as-synthesized ZnO samples were immersed into 0.3 mM N719 dye solution in acetonitrile/tert-butanol (1:1 vol.) and incubated for at least 24 h.

2.4 Solar cell assembly and characterization On the top of the photoanode 25 nm Pt-coated glass (cathode) was placed, thermoplastic was used as a spacer between two electrodes, and I^-/I_3^- electrolyte was sandwiched between two electrodes. Photovoltaic current–voltage (*I–V*) measurements of the solar cells were taken from the circular active area of 0.09π cm^2 (c.a 0.28 cm^2). A Newport full-spectrum solar simulator with Air Mass (AM) 1.5G filter from Oriel was used as a light source in *I–V* measurements. Simulator was operated at the following parameters: AM 1.5G, 100 mW cm^{-2} and 25 °C. Solar cell was illuminated from transparent FTO side.

2.5 ICP-MS measurements Thermo X series II inductively coupled plasma-mass spectrometer (ICP-MS) was used to analyze metal ion concentrations. N719 dye was desorbed from TiO_2 and ZnO surfaces by dilute aqueous ammonia; desorbed dye was then digested in 4 mL of aqua regia (HNO_3:HCl = 1:3). Prior to ICP-MS analysis, samples were diluted by 2% aqueous HCl. Adsorbed N719 amounts were back calculated based on ruthenium concentration. TiO_2 was dissolved in 5 mL of mixture of conc. HNO_3 and HF (4:1), and ZnO was dissolved in 1 mL of conc. HNO_3. Prior to analysis, samples were diluted by 2% aqueous HNO_3. Deposited metal oxide amounts were back calculated based on zinc and titanium concentrations.

3 Results and discussion A three-dimensional nanofibrous template formed by self-assembling peptide amphiphile molecules was used in deposition of TiO_2 and ZnO with varying thickness. As a proof of principle, deposited TiO_2 and ZnO were utilized in dye-sensitized solar cell (DSSC) fabrication and effect of metal oxide layer thickness on cell parameters was studied. For this purpose, the self-assembling peptide amphiphile with the sequence lauryl-VVAGK-Am was synthesized (Scheme 1a). The PA molecules self-assemble into nanofiber network under basic conditions. Self-assembly of the peptide amphiphile molecules into nanofiber in water leads to gel formation; gel is composed of three-dimensional PA nanofiber network entrapping the solvent (Scheme 1b). Removal of the solvent with minimal damage to PA nanonetwork enables one to obtain highly porous organic template (Scheme 1c). Transformation of hydrogel to aerogel is achieved by critical point drying technique. Obtained aerogel was used as a template and coated with TiO_2 (Figs. S4, S5, Supporting Information (SI), online at: www.pss-a.com) and ZnO (Fig. 1d–f, Fig. 2d–f) of different thickness. Energy dispersive X-ray (EDX) spectroscopy verified TiO_2 and ZnO coatings based on presence of Ti or Zn and O atoms; C and N atoms pertaining to organic template were also registered (Figs. S7 and S8 (SI)). After calcination, hybrid

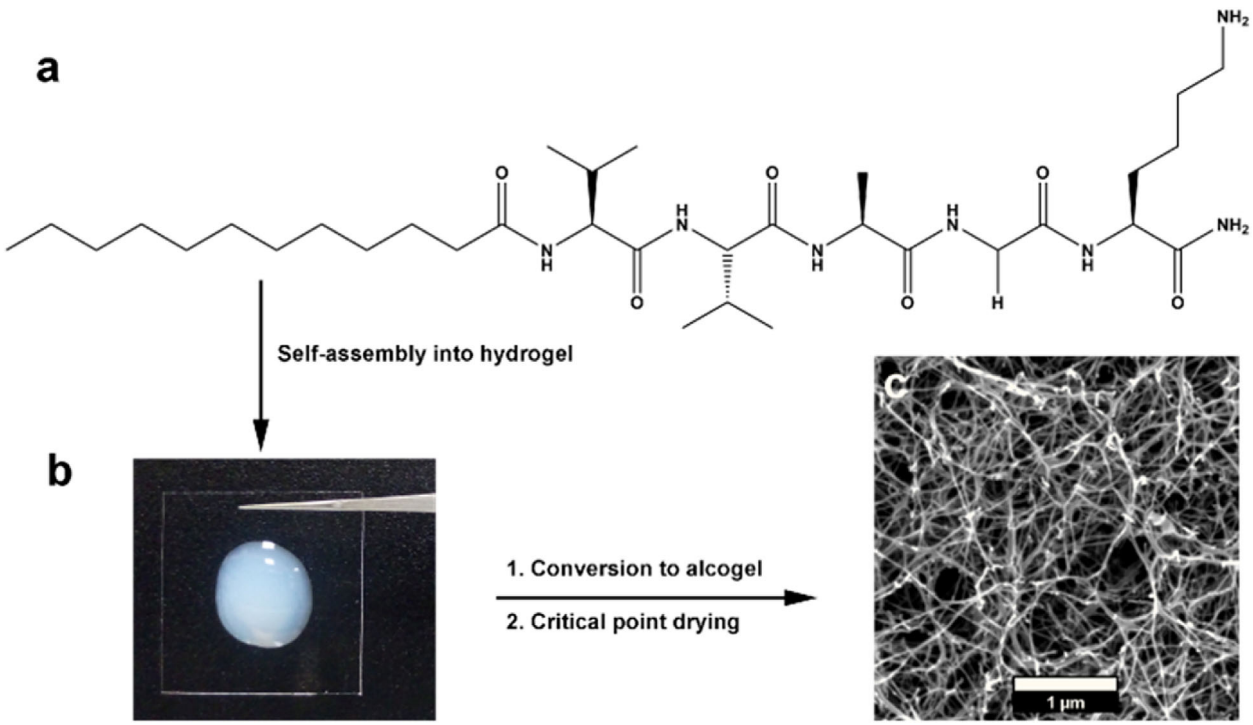

Scheme 1 Fabrication of nanostructured peptide template. (a) Lauryl-VVAGK-Am peptide amphiphile molecule, (b) hydrogel on a cover slip, and (c) SEM image of peptide aerogel.

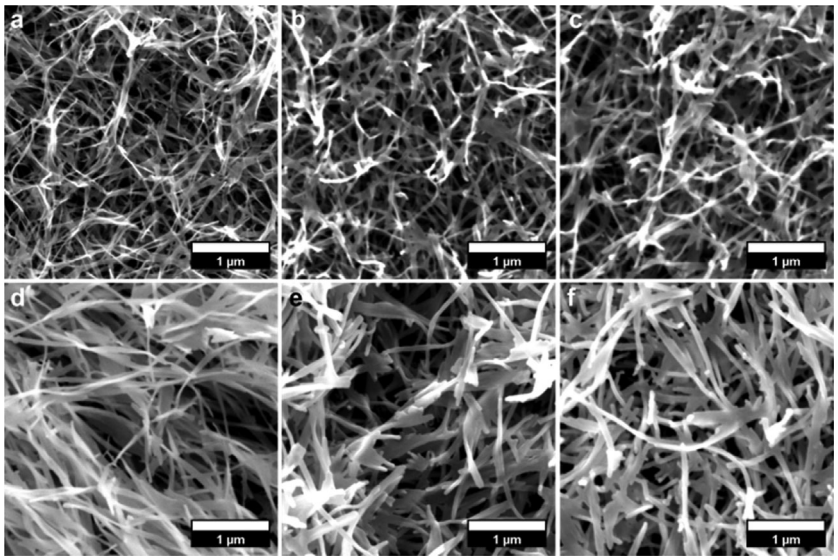

Figure 1 SEM images of (a) 100-cycle, (b) 150-cycle, and (c) 200-cycle TiO_2 nanonetworks after calcination, (d) 100-cycle, (e) 125-cycle, and (f) 150-cycle ZnO nanonetworks.

100, 150, and 200-cycle TiO_2 materials result in nanotube networks (Fig.1a–c and Fig. 2a–c) with 5.18 ± 0.26, 7.52 ± 0.24, and 10.25 ± 0.49 nm wall thickness, respectively. Calcination process removes the organic template and transforms titania to its anatase form. In order to verify phase transformation, XRD and Raman spectra were recorded. Before calcination, XRD and Raman spectra of as-synthesized TiO_2 materials show that material is highly amorphous with negligible presence of rutile phase (Figs. S9 and S10 (SI)) [14]. After calcination, XRD and Raman spectra (Fig. 3a and c) showed that titania transformed to its anatase form. Alongside with anatase form some presence of brookite titania was detected. An extra peak (121) at $2\theta = 30^\circ$ in XRD spectra and several extra peaks at 246, 323, and 365 cm^{-1} in Raman spectra of calcined TiO_2 materials indicate the presence of brookite form [15]. Calcination was not performed for ZnO materials, which were already crystalline with shell thickness of 17.48 ± 1.10, 20.96 ± 0.89, and 23.39 ± 1.32 nm for 100, 125, and 150 deposition cycles, respectively (Fig. 2d–f). Based on XRD and Raman spectroscopy results (Fig. 3b and d), crystalline ZnO coatings exhibited hexagonal wurtzite crystal phase. Raman spectra of ZnO materials, in addition to standard peaks [16], include a peak at 268 cm^{-1}, which was assigned to nitrogen-related mode (NRM). This mode is thought to arise due to disorder or defects favored in the presence of N [17]. NRM in synthesized ZnO materials can stem from peptide-ZnO interface; the PAs upon self-assembly into nanofibers are expected to expose amino groups of lysine residues on the periphery of the nanofibers. ZnO in its wurtzite form is a wide bandgap semiconductor and is utile for photoanode construction. Morphology of obtained nanostructured TiO_2

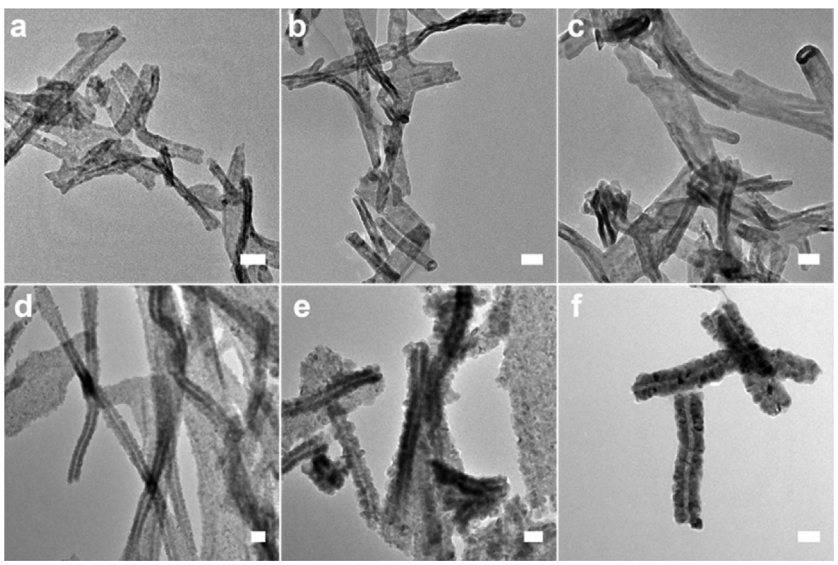

Figure 2 TEM micrographs (a) 100-cycle, (b) 150-cycle, and (c) 200-cycle TiO_2 coated nanofibers after calcination; (d)100-cycle, (e) 125-cycle, and (f) 150-cycle ZnO coated nanofibers. Scale bars are 50 nm.

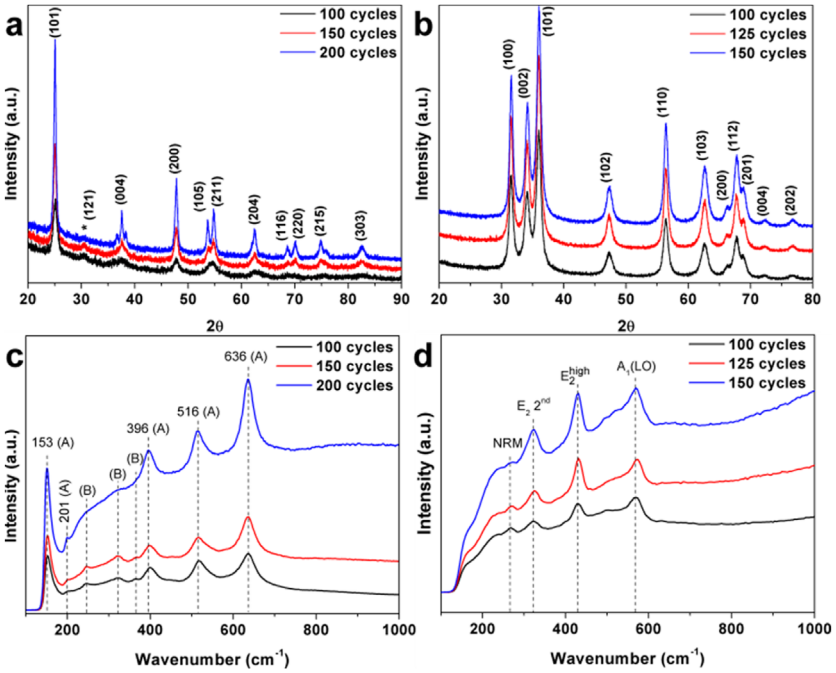

Figure 3 XRD spectra of (a) 100, 150, and 200-cycle TiO_2 and (b) 100, 125, and 150-cycle ZnO; Raman spectra of (c) 100, 150, and 200-cycle TiO_2 and (d) 100, 125, and 150-cycle ZnO. A = anatase, B = brookite.

and ZnO photoanodes was uniform and template effect was preserved throughout the whole anode thickness (Fig. S6). In addition, amorphous TiO_2 readily grew as polymeric material (–Ti–O–), which provided substantially higher surface smoothness; whereas ZnO tended to grow in the form of discrete crystallites, which merged with increasing number of ALD cycles resulting in surface roughness.

$$F(R) = \frac{(1-R)^2}{2R}. \quad (1)$$

For ultra-thin coatings, layer thickness is expected to have an impact on effective material bandgap. To estimate bandgaps (E_g) of nanostructured semiconductor TiO_2 and ZnO materials, diffuse reflectance spectra were recorded. Using the Kubelka–Munk function (Eq. (1)) diffuse reflectance data were transformed into Tauc plots, $(h\nu F(R))^{1/n}$ versus hν, (Fig. 4) with an assumption of direct allowed electron transfer ($n = 0.5$) [18]; R in the equation stands for an absolute reflectance. As-synthesized TiO_2 samples have estimated bandgap values of 3.41, 3.31, and 3.28 eV for 100, 150, and 200 deposition cycles, respectively (Fig. 4a). As expected for nanomaterials, E_g increases as material becomes thinner ($E_{g100} >> E_{g150} > E_{g200}$). Thinner material imposes greater quantum confinement on electron transfer, hence bandgap widening is observed. Surprisingly, calcination led to reversal of order of estimated E_g values ($E_{g100} << E_{g150} < E_{g200}$); the new values are 2.80, 3.21, and 3.23 eV for 100, 150, and 200 cycles, respectively (Fig. 4b). Based on the presence of residual carbon in EDX spectra (Fig. S11 (SI)) of the calcined samples, it can be speculated that thermally decomposing organic template introduces impurities into the material (Fig. S11); the thinnest material (100 cycle TiO_2) is the most affected one. Lee et al. *in silico* studied the electronic properties of C- and N-doped titania [19]. Based

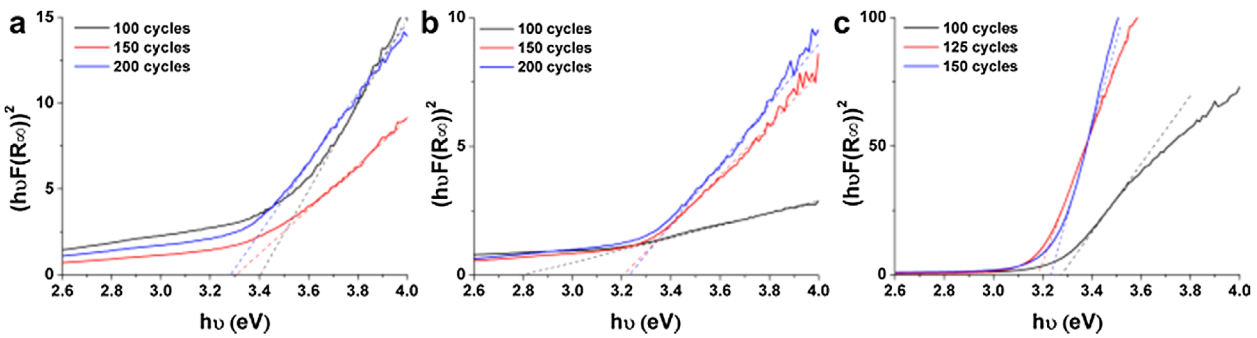

Figure 4 Tauc plots of (a) as-synthesized TiO_2, (b) calcined TiO_2, and (c) ZnO.

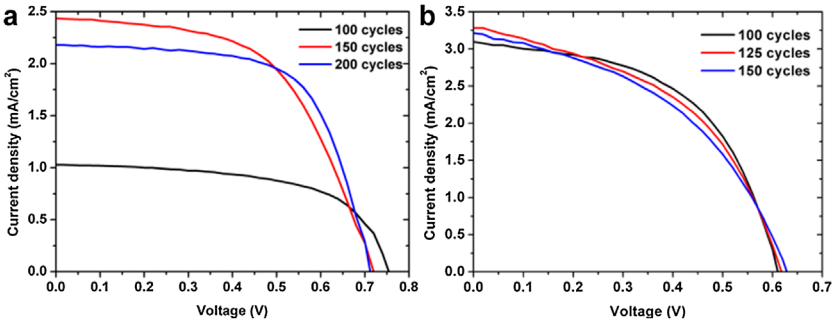

Figure 5 *J–V* curves of (a) 100, 150, and 200-cycle TiO_2 devices, (b) 100, 125, and 150-cycle ZnO devices.

on first-principles density-functional calculations, it was proposed that the red shift in optical absorption of doped material is caused by the presence of isolated C 2p states in the band gap of TiO_2 rather than by a band gap narrowing. Interaction between C impurity atoms and neighboring Ti atoms due to coupling of the top most C 2p state with Ti 4d state is relatively stronger than in N-doped TiO_2. Xu et al. also reported similar results, band structural studies revealed that the visible light activity is related to the isolated impurity states in the band gap [20]. In the case of ZnO, estimated bandgaps were 3.27, 3.18, and 3.24 eV for 100, 125, and 150 cycle ZnO materials, respectively (Fig. 4c). It is clear that estimated bandgaps of relatively thick conformal ZnO layers did not show a linear dependence on cycle number, hence material thickness.

Current density vs. voltage (*J–V*) curves of devices constructed from the obtained materials demonstrate that material thickness has its impact on device parameters (Fig. 5). Hundred-cycle titania sample demonstrated superior V_{oc} compared to 150- and 200-cycle titania ($V_{oc\ 100} >> V_{oc\ 150} > V_{oc\ 200}$) (Fig. 5a). Despite this fact, J_{sc} was inferior for 100-cycle titania. Table 1 summarizes *J–V* parameters for fabricated TiO_2-based DSSC devices. It is clear that device with 150 cycles of TiO_2 deposition is optimal as it is close to 200-cycle device in terms of efficiency, although it possesses less deposited material. The efficiency of 100-cycle device is inferior to 150- and 200-cycle devices, which perform about two times better. Thicker titania nanostructures owing to their higher surface area can accommodate greater number of sensitizer molecules. ICP-MS analysis has shown that adsorbed sensitizer molecule amounts were as 5.89, 9.40, and 13.75 μg for 100, 150, and 200 cycles, respectively; deposited TiO_2 was also cycle-dependent and below 0.2 mg (Table S1, SI). Devices fabricated from nanostructured ZnO have shown similar performance in terms of efficiency (Fig. 5b and Table 1); close V_{oc} and J_{sc} values were observed. Based on ICP-MS results, adsorbed sensitizer amounts were also similar, 391.36, 403.47, and 399.30 μg for 100, 125, and 150 cycles of ZnO deposition, respectively; on contrary, deposited ZnO was cycle-dependent and close to 1 mg (Table S2, SI). The main difference for ZnO devices was in fill factor values; a 100-cycle ZnO device had the highest fill factor, which actually provided higher efficiency for the device. Based on material-efficiency ratio, 100-cycle device is an optimal one among ZnO devices.

Table 1 Cell parameters of nanostructured TiO_2 and ZnO devices.

material	V_{oc} (V)	J_{sc} (mA cm^{-2})	FF	η
100-cycle TiO_2	0.755	1.026	0.60	0.47
150-cycleTiO_2	0.720	2.413	0.56	0.97
200-cycle TiO_2	0.713	2.162	0.65	1.00
100-cycle ZnO	0.610	3.098	0.53	1.01
125-cycle ZnO	0.620	3.284	0.47	0.96
150-cycle ZnO	0.630	3.213	0.44	0.90

Devices based on TiO_2 and ZnO nanonetworks have demonstrated competing efficiencies, although TiO_2 nanonetworks had higher dependence on material thickness. Taking into account amounts of deposited metal oxide and adsorbed dye, TiO_2-based devices substantially outperform ZnO-based ones. Moreover, TiO_2 nanonetworks surpassed ZnO nanonetworks in terms of structural integrity, because ZnO nanonetworks with the same material thicknesses (33, 50, 67 cycles) could not be utilized in functional devices due to disintegration of the networks in I^-/I_3^- electrolyte; therefore, thicker ZnO nanostructures were deposited. Nevertheless, ZnO nanonetworks demonstrated superior dye adsorption properties, which can be utilized in TiO_2-ZnO core shell nanostructured photoanodes.

4 Conclusions Self-assembled peptide amphiphile nanonetwork was successfully used as a template for fabrication of nanostructured TiO_2 and ZnO materials. The template was coated with TiO_2 and ZnO of varying thickness by atomic layer deposition technique. For TiO_2 based devices, we observed that material thickness has prominent effects on device parameters and overall performance. The thinnest material (100 cycles) has demonstrated enhanced V_{oc}, although generated photocurrent was inferior to those of thicker materials. Material thickness affects effective band gap of final metal-oxide layers, which correlates with observed V_{oc} values. Thicker nanostructures (150 and 200 cycles) with higher TiO_2 content adsorbed greater amounts of sensitizer molecules, which resulted in higher photocurrents. Among thicker material devices, 150-cycle device is the optimal one, as it

possesses similar efficiency to 200-cycle device with less deposited titania and less-adsorbed sensitizer. Devices fabricated from nanostructured ZnO have shown similar performance in terms of efficiency. Efficiencies were similar and slightly decreased with increasing cycle number. Devices demonstrated close V_{oc} and J_{sc} values, based on material-efficiency ratio and higher fill factor, 100-cycle ZnO device exhibited optimal device performance. Substantially, higher dye loading observed for ZnO nanonetworks gives an opportunity to boost efficiency of TiO_2-based devices in TiO_2-ZnO core-shell design with just a few ZnO deposition cycles. To best of our knowledge, this is the first report demonstrating fabrication of anodic materials on self-assembled peptide amphiphile template by ALD. This is an inspiring example for biomimetic materials in nanofabrication field.

Supporting Information Additional supporting information may be found in the online version of this article at the publisher's web-site.

Acknowledgements We are thankful to the Scientific and Technological Research Council of Turkey (TUBITAK) for BİDEB 2215 fellowship and 112M578 grant. RG was partially supported by RFBR (grant 16-33-60146) and Program of Competitive Growth of Kazan Federal University.

References

[1] P. Iqbal, J. A. Preece, and P. M. Mendes, Nanotechnology: The "Top-Down" and "Bottom-Up" Approaches, Supramolecular Chemistry: From Molecules to Nanomaterials (John Wiley & Sons, Inc., Hoboken, New Jersey, 2012).
[2] H.-D. Yu, M. D. Regulacio, E. Ye, and M.-Y. Han, Chem. Soc. Rev. **42**, 6006 (2013).
[3] W. E. G. Müller, Molecular Biomineralization: Aquatic Organisms Forming Extraordinary Materials (Springer, Berlin Heidelberg, 2011).
[4] M. B. Dickerson, K. H. Sandhage, and R. R. Naik, Chem. Rev. **108**, 4935 (2008).
[5] J. D. Hartgerink, E. Beniash, and S. I. Stupp, Science **294**, 1684 (2001); H. Acar, R. Garifullin, and M. O. Guler, Langmuir **27**, 1079 (2011); E. D. Sone, S. I. Stupp, Chem. Mater. **23**, 2005 (2011); M. A. Khalily, O. Ustahuseyin, R. Garifullin, R. Genc, and M. O. Guler, Chem. Commun. **48**, 11358 (2012).
[6] H. Acar, R. Garifullin, L. E. Aygun, A. K. Okyay, and M. O. Guler, J. Mater. Chem. A **1**, 10979 (2013).
[7] H. Ceylan, C. Ozgit-Akgun, T. S. Erkal, I. Donmez, R. Garifullin, A. B. Tekinay, H. Usta, N. Biyikli, and M. O. Guler, Sci. Rep. **3**, 2306 (2013).
[8] Q. Zhang and G. Cao, Nano Today, **6**, 91, (2011); T. Prakash, Electron. Mater. Lett. **8**, 231 (2012).
[9] M. Grätzel, J. Photoch. Photobio. C **4**, 145 (2003); W.-Q. Wu, H.-S. Rao, Y.-F. Xu, Y.-F. Wang, C.-Y. Su, and D.-B. Kuang, Sci. Rep. **3**, 1892 (2013); J. H. Park, T.-W. Lee, and M. G. Kang, Chem. Commun. 2867 (2008).
[10] J. B. Baxter and E. S. Aydil, Sol. Energ. Mat. Sol. C **90**, 607 (2006); M. McCune, W. Zhang, Y. Deng, Nano Lett. **12**, 3656 (2012).
[11] S. Gubbala, V. Chakrapani, V. Kumar, and M. K. Sunkara, Adv. Funct. Mater. **18**, 2411 (2008); S. Gubbala, H. B. Russell, H. Shah, B. Deb, J. Jasinski, H. Rypkema, and M. K. Sunkara, Energy Environ. Sci. **2**, 1302 (2009).
[12] A. Le Viet, R. Jose, M. V. Reddy, B. V. R. Chowdari, and S. Ramakrishna, J. Phys. Chem. C **114**, 21795 (2010); R. Ghosh, M. K. Brennaman, T. Uher, M.-R. Ok, E. T. Samulski, L. E. McNeil, T. J. Meyer, and R. Lopez, ACS Appl. Mater. Interfaces **3**, 3929 (2011).
[13] X. Lu, S. Ding, T. Lin, X. Mou, Z. Hong, F. Huang, and T. Dalton, **41**, 622 (2012); D. Gompel, M. N. Tahir, M. Panthofer, E. Mugnaioli, R. Brandscheid, U. Kolb, and W. Tremel, J. Mater. Chem. A **2**, 8033 (2014).
[14] U. Balachandran and N. G. Eror, J. Solid State Chem. **42**, 276 (1982).
[15] G. A. Tompsett, G. A. Bowmaker, R. P. Cooney, J. B. Metson, K. A. Rodgers, and J. M. Seakins, J. Raman Spectrosc. **26**, 57 (1995); D. Bersani, G. Antonioli, P. P. Lottici, and T. Lopez, J. Non-Cryst. Solids **232–234**, 175 (1998).
[16] C. A. Arguello, D. L. Rousseau, and S. P. S. Porto, Phys. Rev. **181**, 1351 (1969).
[17] L. Artús, R. Cuscó, E. Alarcón-Lladó, G. González-Díaz, I. Mártil, J. Jiménez, B. Wang, and M. Callahan, Appl. Phys. Lett. **90**, 181911 (2007).
[18] E. L. Simmons, Appl. Opt. **14**, 1380 (1975).
[19] J.-Y. Lee, J. Park, and J.-H. Cho, Appl. Phys. Lett. **87**, 011904 (2005).
[20] T.-H. Xu, C.-L. Song, Y. Liu, and G.-R. Han, J. Zhejiang Univ. – Sci. B **7**, 299 (2006).

